



**HAL**  
open science

# A simplified 3D oceanic model assimilating geostrophic currents: Application to the POMME experiment

H Giordani, G Caniaux, L Prieur

► **To cite this version:**

H Giordani, G Caniaux, L Prieur. A simplified 3D oceanic model assimilating geostrophic currents: Application to the POMME experiment. *Journal of Physical Oceanography*, 2005, 35 (5), pp.628-644. 10.1175/JPO2724.1 . hal-03494215

**HAL Id: hal-03494215**

**<https://hal.science/hal-03494215>**

Submitted on 24 Dec 2021

**HAL** is a multi-disciplinary open access archive for the deposit and dissemination of scientific research documents, whether they are published or not. The documents may come from teaching and research institutions in France or abroad, or from public or private research centers.

L'archive ouverte pluridisciplinaire **HAL**, est destinée au dépôt et à la diffusion de documents scientifiques de niveau recherche, publiés ou non, émanant des établissements d'enseignement et de recherche français ou étrangers, des laboratoires publics ou privés.



Distributed under a Creative Commons Attribution 4.0 International License

## A Simplified 3D Oceanic Model Assimilating Geostrophic Currents: Application to the POMME Experiment

HERVÉ GIORDANI, GUY CANIAUX, AND LOUIS PRIEUR

*Météo-France, Toulouse, France*

(Manuscript received 6 October 2003, in final form 9 November 2004)

### ABSTRACT

A simplified oceanic model is developed to easily perform cheap and realistic mesoscale simulations on an annual scale. This simplified three-dimensional oceanic model is obtained by degenerating the primitive equations system by prescribing continuously analysis-derived geostrophic currents  $\mathbf{U}_g$  into the momentum equation in substitution of the horizontal pressure gradient. Simplification is provided by a time sequence of  $\mathbf{U}_g$  called guide, which is used as a low-resolution and low-frequency interpolator. This model is thus necessarily coupled to systems providing geostrophic currents—that is, ocean circulation models, analyzed/reanalyzed fields, or climatologies. In this model, the mass and currents fields are constrained to adjust to the geostrophic guide at all scales. The vertical velocity is deduced from the vorticity equation, which ensures the coherence between the vertical motion and the geostrophic structures evolution. Horizontal and vertical advection are the coupling processes that can be activated independently from each other and offer the possibility to (i) continuously derive a three-dimensional model when all processes are activated, (ii) understand how some retroaction loops are generated, and (iii) study development of structures as a function of the geostrophic environment. The model was tested during a 50-day lasting simulation over the Program Océan Multidisciplinaire Méso Echelle (POMME) experiment (northeast Atlantic Ocean, September 2000–October 2001). Optimal analyzed geostrophic currents were derived weekly during POMME from a quasigeostrophic model assimilating altimeter data. Comparison with independent in situ and satellite data indicates that this simulation is very realistic and does not drift, thanks to the prescribed geostrophic guide.

### 1. Introduction

The Program Océan Multidisciplinaire Méso Echelle experiment (POMME; Mémerly et al. 2005, manuscript submitted to *EOS, Trans. Amer. Geophys. Union*) took place in the northeast Atlantic Ocean off Portugal half way between the Azores and the Iberian Peninsula from early September 2000 to late September 2001 (Fig. 1). During this period, a multiparameter dataset was collected at a high spatial and temporal resolution in the POMME area in order to understand the impact of mesoscale structures (around 50–200 km) on processes of 11°–13°C mode water subduction (Paillet and Arhan 1996), mixed layer heat and mass budgets, and the spring bloom.

To understand the processes at play in the formation and circulation of mode water at the mesoscale in the POMME area, it is necessary to implement a three-dimensional oceanic model. So as to capture the realistic evolution of the mesoscale structures, especially

over monthly or annual periods for subduction studies, such a model needs to be coupled to a data assimilation system (Robinson 1996). The majority of models use sequential assimilation systems, which are efficient in reducing drift but induce mass-circulation imbalances at each reinitialization procedure. Such imbalances produce shocks and the radiation of spurious gravity waves that are inappropriate for estimating physical diagnoses and time-integrated mixed layer budgets (Gavart 1996; Gavart and De Mey 1997). Moreover, Gavart (1996) has also found evidence of temporal degradation of the simulations induced by the lateral boundaries. These results illustrate well the difficulty of performing realistic annual-long simulations with a regional high-resolution primitive equation (PE) model.

Alternative simplified approaches were developed in the literature and successfully applied even in regions where advective terms are important. For instance, Qiu and Kelly (1993) have developed a simplified horizontal two-dimensional integral mixed layer model including horizontal advection of temperature in order to study the upper-ocean heat balance in the Kuroshio frontal region during a period of 2.5 yr. The success of their approach is due to reliable representations of the Ekman and mainly geostrophic flow. Based on a mean

---

*Corresponding author address:* Hervé Giordani, Centre National de Recherches Météorologiques, 42 av. G. Coriolis, 31057 Toulouse, France.  
E-mail: herve.giordani@meteo.fr

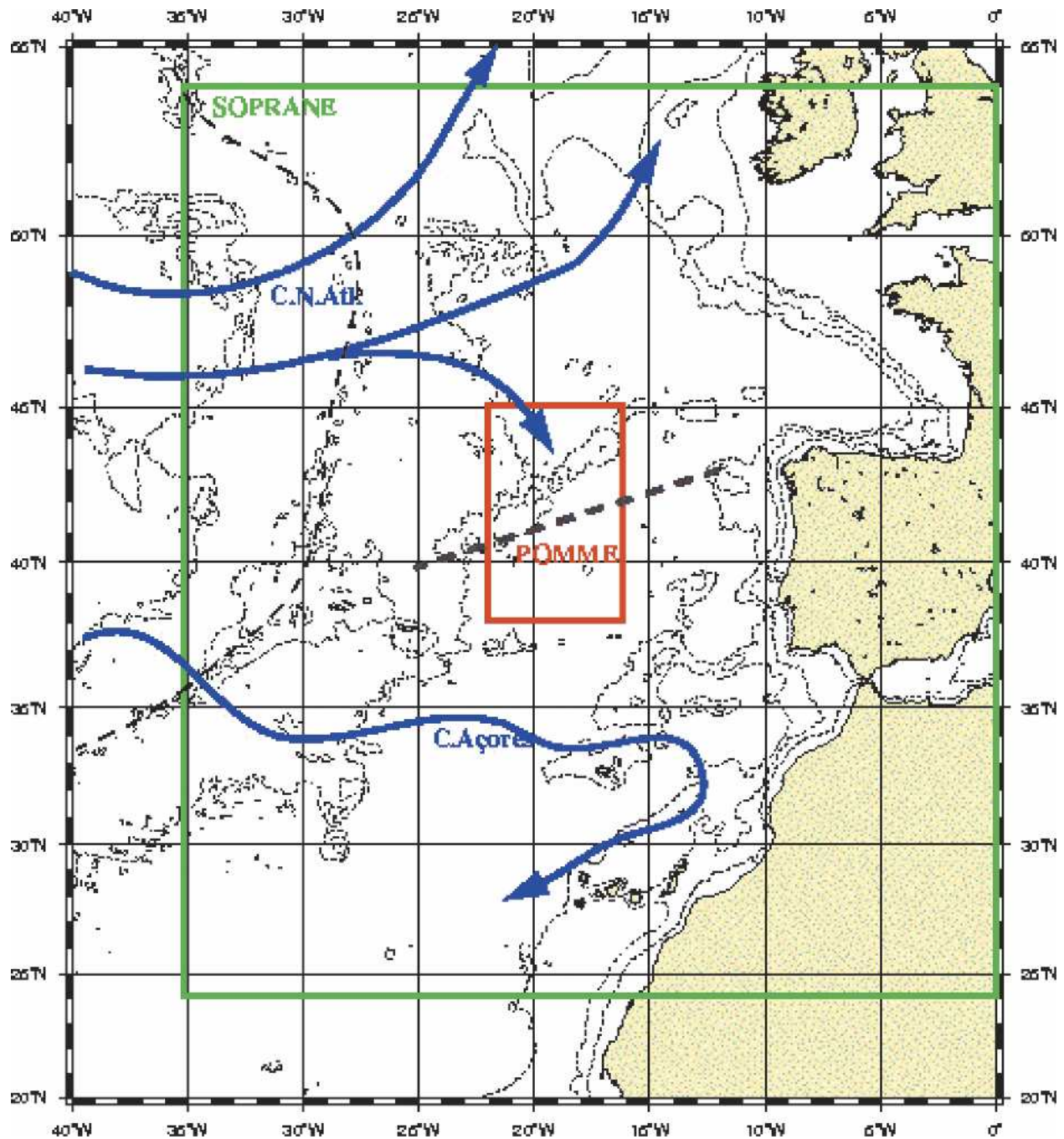


FIG. 1. Positioning of the POMME experiment. Small rectangle represents the experimental and simulation domain. Large rectangle represents the simulation domain of the quasigeostrophic model SOPRANE. Dashed line crossing the POMME domain symbolizes the climatological place where the mode water subduction occurs.

surface height field, *Geosat* altimetric measurements, and an objective analysis method, Qiu et al. (1991) obtained analyzed gridded absolute surface heights in the Kuroshio region. Geostrophic flow was derived from these analyzed surface heights and was used to compute integral horizontal advection in the Qiu and Kelly (1993) model. This example shows that the introduction

or assimilation of geostrophic currents into a simplified model is still an efficient approach in order to capture the essential dynamics and thermodynamics of the mixed layer over long periods. This approach helped these authors to clarify the role played by current advection (geostrophic–Ekman) in determining the upper-ocean heat balance.

Usually, hydrographic data are preferentially assimilated in comparison with velocity data because of their greater availability. Nevertheless some work exists on velocity data assimilation, and Robinson (1996) has demonstrated that the forecast fields in the northwest Atlantic are strongly different when mass and/or velocity are assimilated into a PE model. Specifically, meso-scale structures are better forecast when velocity fields are assimilated.

The purpose of this paper is to develop and validate a simplified three-dimensional oceanic model assimilating geostrophic currents analyses. The approach is largely inspired by Qiu and Kelly (1993) but the method used to assimilate geostrophic currents into the model differs. A data direct-insertion method described in Robinson et al. (1998) is used in Qiu and Kelly (1993), but in ours (i) the geostrophic currents are inserted gradually—that is, a smooth assimilation technique corresponding to a data-driven procedure (Lozano et al. 1996; Robinson et al. 1998) is used—and (ii) geostrophic currents are directly assimilated into the momentum equation by replacing the horizontal pressure force. The latter is a fundamental difference with Qiu and Kelly's (1993) method because the proposed approach allows for geostrophic adjustment.

The proposed numerical tool aims to simulate meso-scale and submesoscale structures over a period of about a year in order to give detailed mixed layer heat and subduction budgets in the POMME area. Nevertheless, these are the objectives of a forthcoming paper and the present paper is only devoted to the presentation and validation of the model. Sensitivity tests based on 50-day-long simulations during the POMME experiment are also presented.

## 2. Formulation of the model

The strategy adopted to derive a 3D oceanic model is to start from the vertical ( $z$ ) 1D mixed layer model developed by Gaspar et al. (1990). In the one-dimensional case, the conservation of heat, salt, and momentum yields the following mixed layer (ML) system:

$$\begin{aligned} \frac{\partial \mathbf{U}_h}{\partial t} &= -f\mathbf{k} \times \mathbf{U}_h + \frac{\partial}{\partial z} \left( K \frac{\partial \mathbf{U}_h}{\partial z} \right), \\ \frac{\partial T}{\partial t} &= \frac{F_{\text{sol}}}{\rho C_p} \frac{\partial I(z)}{\partial z} + \frac{\partial}{\partial z} \left( K \frac{\partial T}{\partial z} \right), \quad \text{and} \\ \frac{\partial S}{\partial t} &= \frac{\partial}{\partial z} \left( K \frac{\partial S}{\partial z} \right), \end{aligned} \quad (1)$$

where  $T(z)$ ,  $S(z)$ , and  $\mathbf{U}_h[u(z), v(z)]$  are the temperature, salinity, and horizontal velocity;  $\rho$  and  $C_p$  are the density and specific heat of seawater;  $I(z)$  is the fraction of the net solar surface irradiance  $F_{\text{sol}}$  that penetrates to depth  $z$ ;  $f$  is the Coriolis parameter;  $K$  is the vertical mixing coefficient; and  $\mathbf{k}$  is the vertical unit vector.

The turbulent vertical mixing parameterization is based on a parameterization of the second-order turbulent moments expressed as a function of the turbulent kinetic energy  $e_T$ , which is given by prognostic Eq. (2):

$$\frac{\partial e_T}{\partial t} = \frac{\partial}{\partial z} \left( K \frac{\partial e_T}{\partial z} \right) + K \left( \frac{\partial \mathbf{U}_h}{\partial z} \right)^2 + \frac{g}{\rho} K \frac{\partial \rho}{\partial z} - C_\epsilon \frac{e_T^{3/2}}{l_\epsilon}, \quad (2)$$

where  $C_\epsilon$  is a constant,  $l_\epsilon$  is a characteristic dissipation length, and  $g$  is the gravity. In this formulation, the  $K$ s are based on the calculation of two turbulent length scales representing upward and downward conversions of turbulent kinetic energy into potential energy (Bougeault and Lacarrère 1989). Such a scheme was shown to improve vertical mixing in the tropical Atlantic Ocean owing to high frequencies in surface forcing, and the scheme thereby improved the representation of the vertical mixed layer structure, sea surface temperature, and upper-layer current (Blanke and Delecluse 1993). However, several authors have pointed out that this parameterization fails to properly simulate the mixing in strongly stable layers like the upper thermocline (Large et al. 1994; Kantha and Clayson 1994). Gaspar et al. (1990) tried to simulate the evolution of the mixed layer using the Long-Term Upper-Ocean Study (LOTUS) dataset. After computing a mixed layer heat budget with their model, they found an important heat deficit in comparison with the observations. They attributed this deficit to surface heat fluxes, whereas the misfit was probably due to a deficiency of vertical mixing at lower levels of the mixed layer as indicated by Large et al. (1994).

Consequently, a parameterization of the diapycnal mixing (Large et al. 1994) was introduced in Gaspar's model in order to take into account the effects of the vertical mixing occurring in the thermocline (Josse 1999). This nonlocal source of mixing, mainly due to internal waves breaking and current shear between the mixed layer and upper thermocline, is able to affect the temperature, salinity, momentum, and turbulent kinetic energy inside the mixed layer, particularly during restratification periods.

Formally, the one-dimensional ML model can be three-dimensionalized by adding independent modules to the system that couple the vertical columns between them. These coupling modules are the horizontal pressure force, horizontal/vertical advections in the momentum equation, and horizontal/vertical advections in the temperature and salinity equations. Last, an equation of seawater state and the hydrostatic equation for the vertical momentum are needed to complete the 3D system. The nonlinear coupling operator (CO) that three-dimensionalizes the system ML is then written as follows:



$$\begin{aligned} \frac{\partial \mathbf{U}_h}{\partial t} &= -\frac{1}{\rho} \nabla_h P - (\mathbf{U} \cdot \nabla) \cdot \mathbf{U}_h, \\ \frac{\partial T}{\partial t} &= -(\mathbf{U} \cdot \nabla T), \\ \frac{\partial S}{\partial t} &= -(\mathbf{U} \cdot \nabla S), \\ \frac{\partial P}{\partial z} &= -\rho g, \quad \text{and} \\ \rho &= \rho(T, S), \end{aligned} \tag{3}$$

where  $\mathbf{U} = (u, v, w)$  and  $P$  are the total current and pressure, respectively. The model (ML + CO) represents the PE model, which has four prognostic variables: horizontal current  $\mathbf{U}_h = (u, v)$ , temperature  $T$ , and salinity  $S$ . In the “ $x, y, z$ ” coordinate frame, their evolutions are expressed by the following:

$$\begin{aligned} \frac{\partial \mathbf{U}_h}{\partial t} &= -\frac{1}{\rho} \nabla_h P - f \mathbf{k} \times \mathbf{U}_h + \frac{\partial}{\partial z} \left( K \frac{\partial \mathbf{U}_h}{\partial z} \right) \\ &\quad - (\mathbf{U} \cdot \nabla) \times \mathbf{U}_h, \\ \frac{\partial T}{\partial t} &= \frac{F_{\text{sol}}}{\rho C_p} \frac{\partial I(z)}{\partial z} + \frac{\partial}{\partial z} \left( K \frac{\partial T}{\partial z} \right) - (\mathbf{U} \cdot \nabla T), \\ \frac{\partial S}{\partial t} &= \frac{\partial}{\partial z} \left( K \frac{\partial S}{\partial z} \right) - (\mathbf{U} \cdot \nabla S), \\ \frac{\partial P}{\partial z} &= -\rho g, \quad \text{and} \\ \rho &= \rho(T, S). \end{aligned} \tag{4}$$

To close the system of equations in Eq. (4) an equation of vertical velocity  $w$  is needed. This point will be addressed in section 2a.

Rosati and Miyakoda (1988) and Gaspar et al. (1990) found that horizontal advection and diffusion terms play a minor role in the three-dimensional turbulent kinetic energy budget. Consequently, Eq. (2) was not modified.

a. Vertical velocity

Another important point is to use a formulation that gives access to vertical velocity ( $w$ ) sources in order to quantify the relative part of physical processes acting in the mode water subduction. For such studies, several authors (Viùdez et al. 1996; Giordani and Planton 2000) suggest using an  $\omega$  equation rather than the continuity equation, but this approach is heavy to be integrated online into a model and was abandoned for the time being.

Even though the vertical velocity can be straightforwardly inferred from the continuity equation, this method is not to be recommended because the horizontal divergence is due primarily to the small departures of the current from the geostrophic balance. An error of 10% in a current component can easily cause

error of 100% in estimated divergences using finite difference approximations (Holton 1979). Moreover, in our case, the geostrophic current is not strictly nondivergent because of errors in the data and those associated with the computing method that induce spurious signals in the vertical motion. In such cases, Holton (1979) and Pedlosky (1987) suggest deriving the vertical velocity from the vorticity equation:

$$\begin{aligned} \frac{d(\zeta + f)}{dt} &= \underbrace{-(\zeta + f) \nabla_h \cdot \mathbf{U}_h}_{\text{Divergence term}} + \underbrace{\frac{\mathbf{k}}{\rho^2} \cdot (\nabla_h \rho \times \nabla_h P)}_{\text{Baroclinic term}} \\ &\quad + \underbrace{\mathbf{k} \cdot \left( \frac{\partial \mathbf{U}_h}{\partial z} \times \nabla_h w \right)}_{\text{Tilting term}} - \underbrace{\frac{\mathbf{k}}{\rho} \text{Rot} \left( \frac{\partial \boldsymbol{\tau}}{\partial z} \right)}_{\text{Stress term}}. \end{aligned} \tag{5}$$

Using the continuity equation  $\nabla_h \cdot \mathbf{U}_h + \partial w / \partial z = 0$  it is then possible to extract the vertical velocity from the divergence term:

$$\begin{aligned} \frac{\partial w}{\partial z} &= \frac{1}{(\zeta + f)} \left[ \underbrace{\frac{\partial(\zeta + f)}{\partial t}}_{\text{Local Trend of Vorticity}} + \underbrace{\mathbf{U} \cdot \nabla(\zeta + f)}_{\text{Advection of Vorticity}} \right] \\ &\quad + \frac{1}{(\zeta + f)} \left[ \underbrace{\frac{f}{\rho} \mathbf{U}_g \cdot \nabla_h \rho}_{\text{Baroclinic term}} - \underbrace{\mathbf{k} \cdot \left( \frac{\partial \mathbf{U}_h}{\partial z} \times \nabla_h w \right)}_{\text{Tilting term}} \right] \\ &\quad + \underbrace{\frac{\mathbf{k}}{\rho} \text{Rot} \left( \frac{\partial \boldsymbol{\tau}}{\partial z} \right)}_{\text{Stress term}}. \end{aligned} \tag{6}$$

Equation (6) is particularly well suited to establishing a relationship between mesoscale variability and the induced vertical motion, and  $w$  can be interpreted in terms of change of relative vorticity in a fluid parcel (Viùdez et al. 1996).

The local trend and advection of vorticity depending on the first order of the geostrophic current (Holton 1979), the vertical velocity is thus strongly driven by Lagrangian evolution of the geostrophic eddy structures [term  $d\zeta_g/dt =$  geostrophic local trend + geostrophic advection of vorticity in Eq. (6)]. This means that a large part of the vertical velocity is forced by the evolution of the geostrophic mesoscale structures. This part of the ageostrophic circulation corresponds to the geostrophic adjustment of the mesoscale structures. The other part is associated with retroaction of the ageostrophic circulation on itself [term  $d\zeta_{ag}/dt =$  ageostrophic local trend + ageostrophic advection of vorticity in Eq. (6)]. The tilting term is associated with vorticity field deformation and the baroclinic term is the process that adjusts the mass field to the imposed geostrophic current, both of which can be strong in

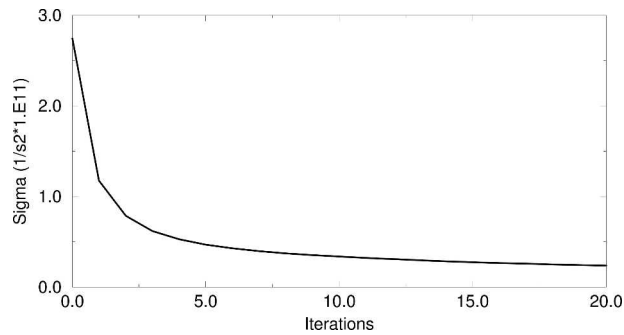


FIG. 2. Standard deviation of the vorticity advection ( $s^{-2} \times 10^{11}$ ) vs the iterations number of the low-pass filter.

frontal and eddy zones where baroclinicity is high. The stress term represents Ekman pumping.

#### TREATMENT OF VORTICITY ADVECTION

Because experimental data and numerical methods were used to derive geostrophic currents, a non-negligible part of noise is present. Unlike the QG models, the system of equations in Eq. (4) does not filter the spurious gravity waves generated by noise contained in the assimilated data. Consequently, the physical signal of the vertical velocity is easily masked by the noise. This problem is well known in operational atmospheric

forecast systems, where normal-modes filters (Machenhauer 1977; Daley 1981; Lynch 1985a,b) or digital filters (Hamming 1989; Lynch 1997) are applied on optimal analyzed fields in order to eliminate numerical gravity waves.

In our case the geostrophic current was not filtered since this solution alters the general circulation and weakens the scalar advectons. An alternative method was to apply a low-pass filter on the vorticity advection term since it is the main source of noise because of its intensity and nonlinear character.

Noise contained in the vorticity advection can be evaluated by computing its standard deviation  $\sigma$ . For example,  $\sigma$  was computed over the analyzed currents of POMME1, and Fig. 2 shows its behavior with respect to the number of iterations of the low-pass filter. During the first 10 iterations,  $\sigma$  decreases rapidly and stabilizes beyond. After 10 and 20 iterations,  $\sigma$  has decreased by 88% and 91% from its initial value, respectively. Numerous tests were performed with other analyzed fields. These tests were confirmed that the value of 10 iterations noticeably removes the noise in the vorticity advection field.

Figure 3 gives an illustration of how the vertical velocity signal is filtered when vorticity advection is also filtered. When the filter fails, the vertical velocity at the surface is very noisy because it includes noise cumulated over the entire column. When the filter works, the

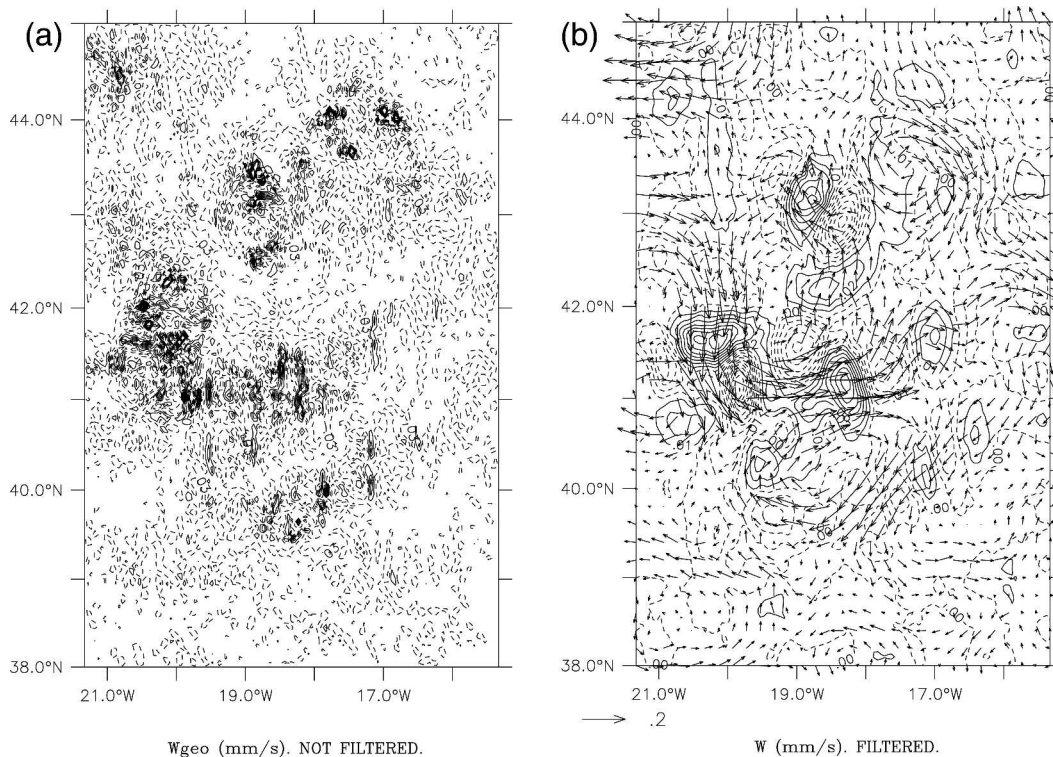


FIG. 3. Surface vertical velocity ( $mm\ s^{-1}$ ) computed from the POMME1 dataset (a) without filtering of the vorticity advection and (b) with filtering of the vorticity advection. Superimposed in (b) is the geostrophic surface current ( $m\ s^{-1}$ ).

structures of  $w$  are coherent and have physical meanings with the surface current. For example, structures of high intensity are found on the tracks of strong currents and the changes of sign are often located where the curvature of current changes. Such a filtering has been applied in the model to compute  $w$ .

### b. Data assimilation strategy

#### ASSIMILATION METHOD AND DEGENERATION OF THE PE SYSTEM

In situ and altimetric satellite data collected during the POMME experiment allowed calculation of optimal analysis (OA) geostrophic currents  $\mathbf{U}_g$  at high frequency and with a 50-km horizontal resolution. Given the unprecedented information given by the analyzed geostrophic currents, an alternative assimilation method of this newly available information into a model is proposed in this paper. This method is largely inspired from the Qiu and Kelly (1993) one.

The central idea of this paper is to simplify the primitive equation set in Eq. (4) (ML + CO) by replacing the horizontal pressure force in the momentum equation with a prescribed geostrophic current  $\mathbf{U}_g$  using the link between  $\mathbf{U}_g$  and  $\nabla_h P$  [ $\mathbf{U}_g = (1/\rho f)\mathbf{k} \times \nabla_h P$ ]. When analyses of geostrophic currents are available, the momentum equation of Eq. (4) can be simplified into the following form:

$$\begin{aligned} \frac{\partial \mathbf{U}_h}{\partial t} = & -f\mathbf{k} \times (\mathbf{U}_h - \mathbf{U}_g) + \frac{\partial}{\partial z} \left( K \frac{\partial \mathbf{U}_h}{\partial z} \right) \\ & - (\mathbf{U} \cdot \nabla) \cdot \mathbf{U}_h. \end{aligned} \quad (7)$$

This operation simplifies the primitive equations system (ML + CO) and induces important simplifications and consequences, which are discussed in section 2c. This assimilation is thus a direct insertion into the model but differs from the Qiu and Kelly (1993) method in some important aspects, which are also explained in section 2c.

In POMME, OA geostrophic currents being avail-

able at high frequency (weekly),  $\mathbf{U}_g$  can be estimated with a good accuracy at each model time step by linear interpolation between two gridded analyzed networks. Interpolated  $\mathbf{U}_g$  are directly inserted into the model that is a gradual and smooth assimilation procedure corresponding to a continuous data-driven simulation. This procedure is not exactly similar to that in Lozano et al. (1996) since insertion is carried out at each model time step and not only around a given time. A direct insertion means that no statistical uncertainties are considered in this assimilation technique. The simplest assimilation technique was intentionally chosen, because this paper focuses on the ability of our model to simulate realistic mesoscale structures under prescribed geostrophic currents in the momentum equation.

More sophisticated assimilation strategies mentioned below could bring significant added values to our approach but are outside the scope of this paper. The OA assimilation schemes melding analyzed geostrophic currents with forecast geostrophic currents could be more appropriate to capture the time and space scales of the real processes of interest (Lozano et al. 1996; Robinson et al. 1998). When ocean data are sparse, the background of initialization is constructed from multiscale feature models (Lozano et al. 1996) that could be used in our model. In OA, the prediction of the model error is usually of empirical form and the error covariances do not take into account the dynamic constraints of the model leading to mass-current imbalances. More advanced methods give a dynamical model of the error covariances, which are in accordance with the model equations (Lermusiaux and Robinson 1999). Such methods could yield refinement of the OA weights and lead to a more robust, efficient, and rapid assimilation system.

### c. Characteristics of the simplified PE system (ML + CO)

#### 1) DIFFERENCES WITH STANDARD MODELS

The complete simplified PE system derived step by step in the previous sections is written as follows:

$$\begin{aligned} \frac{\partial \mathbf{U}_h}{\partial t} = & -f\mathbf{k} \times (\mathbf{U}_h - \mathbf{U}_g) + \frac{\partial}{\partial z} \left( K \frac{\partial \mathbf{U}_h}{\partial z} \right) - (\mathbf{U} \cdot \nabla) \cdot \mathbf{U}_h, \\ \frac{\partial T}{\partial t} = & \frac{F_{\text{sol}}}{\rho C_p} \frac{\partial I(z)}{\partial z} + \frac{\partial}{\partial z} \left( K \frac{\partial T}{\partial z} \right) - (\mathbf{U} \cdot \nabla T), \\ \frac{\partial S}{\partial t} = & \frac{\partial}{\partial z} \left( K \frac{\partial S}{\partial z} \right) - (\mathbf{U} \cdot \nabla S), \\ \frac{\partial e_T}{\partial t} = & \frac{\partial}{\partial z} \left( K \frac{\partial e_T}{\partial z} \right) + K \left( \frac{\partial \mathbf{U}_h}{\partial z} \right)^2 + \frac{g}{\rho} K \frac{\partial \rho}{\partial z} - C_\epsilon \frac{e_T^{3/2}}{l_\epsilon}, \\ \frac{\partial w}{\partial z} = & \frac{1}{(\zeta + f)} \left[ \frac{\partial(\zeta + f)}{\partial t} \right] + \mathbf{U} \cdot \nabla(\zeta + f) + \frac{f}{\rho} \mathbf{U}_g \cdot \nabla_h \rho - \mathbf{k} \cdot \left( \frac{\partial \mathbf{U}_h}{\partial z} \times \nabla_h w \right) + \frac{\mathbf{k}}{\rho} \cdot \text{Rot} \left( \frac{\partial \boldsymbol{\tau}}{\partial z} \right), \quad \text{and} \\ \rho = & \rho(T, S). \end{aligned} \quad (8)$$

The numerical resolution of the system of equations in Eq. (8) is presented in the appendix A.

It is important to note that in the system of equations in Eq. (8),  $\mathbf{U}_g$  is assimilated or directly inserted into the momentum equation with a relaxation frequency equal to the Coriolis parameter: it is not directly prescribed in the total current as in Qiu and Kelly (1993). Assimilation methods are identical but the assimilated variable is not located at the same place. This difference is fundamental because our approach authorizes geostrophic adjustment. This operation eliminates the pressure in Eq. (4) so that the hydrostatic equation becomes unnecessary. Consequently, elimination of the pressure degenerates the PE system. A linearization of Eq. (7) [which is the momentum equation of Eq. (8)] around the assimilated geostrophic base state shows that the waves induced by Eq. (7) are only inertial waves. Consequently, this system generates no gravity waves and the simulated current  $\mathbf{U}_h$  adjusts to  $\mathbf{U}_g$  at the Coriolis frequency.

Quasigeostrophic (QG) models are systems that filter the inertial-gravity waves and ageostrophic motions and that do not take into account the turbulence processes. Conversely, as in QG models, ageostrophic motions are explicitly computed into the proposed simplified model [Eq. (7)]. This point is particularly important to represent realistically three-dimensional dynamics in fronts and in eddies. Last, this simplified model is provided with a vertical mixing parameterization in order to get a representation of the mixed layer.

In this system, the time sequence of  $\mathbf{U}_g$  is used as a low-resolution and low-frequency interpolator that acts as a guide and imposes a large part of the geostrophic adjustment. Note that this model is necessarily attached to a time sequence of  $\mathbf{U}_g$  that is gradually inserted into the momentum equation (see section 2b). In these conditions, this guide gives rise to an ageostrophic circulation ( $\mathbf{U}_{ag} = \mathbf{U}_h - \mathbf{U}_g$ ), which balances the mass fields with the prescribed geostrophic dynamic through the  $T$  and  $S$  equations. The simulated structures correspond to the adjustment of the mass field to this guide, and the important point is that these structures are dynamically consistent with this guide at all scales. In this guided system, geostrophic structures have an action on the ageostrophic structures but not vice versa. In oceanic circulation models (OCM) using nondegenerate PE systems, this coupling is allowed in two ways that lead the momentum and density/pressure fields to adjust themselves through gravity waves developed by the system. The two approaches are distinguished precisely by this point. This guided system could be softened by blending the forecast and OA geostrophic currents in connection with their uncertainties. Uncertainties of the forecast fields could be predicted via an ensemble approach (Lermusiaux 1999). In this case, the ageostrophic structures could have a retroaction on the geostrophic ones.

## 2) CONSEQUENCES OF CURRENT DATA ASSIMILATION

In the shallow-water framework, Bougeault and Sadourny (2001) have shown that the geostrophic adjustment works differently according to scales. For scales smaller (greater) than the Rossby radius ( $R_o$ ), the mass (velocity) field adjusts to the velocity (mass) field. The separating scale between “large” and “small” is  $R_o$ . This result has large implications in meteorology and oceanography. If one focuses on forecasting at scales greater than  $R_o$ , the mass field has to be initialized or prescribed with accuracy. Conversely, a good forecast of scales smaller than  $R_o$  needs an accurate initialization (or prescription in the present case) of the velocity field. This result emphasizes that assimilation of mass or geostrophic current field is not similar in term of forecasting. This point argues for an assimilation of the analyzed geostrophic currents rather than the mass fields in this study because small scales need to be realistically simulated. Particularly, the finer the resolution of the current is, the better the small structures should be simulated. In this study, the resolution of the geostrophic guide is typically of 50 km but its characteristics can be changed, which gives the possibility to study the development of simulated small-scale structures as a function as various mesoscale environments.

Using an intermittent optimal interpolation scheme and a PE model implemented in the northwest Atlantic, Robinson (1996) showed that over 35% improvement was obtained in the forecast fields when the velocity or the geostrophic velocity fields were assimilated. Moreover, when velocity fields were assimilated gradually, improvement increases substantially up to 70%. When only temperature and salinity were assimilated, only 1.5% improvement was obtained. Robinson’s results and theoretical results of Bougeault and Sadourny (2001) are consistent and confirm that small-scale structures are better simulated when velocity fields are assimilated.

## 3) ADVANTAGES AND LIMITATIONS

Generally, the integration of the primitive equations needs to split the total current into barotropic and baroclinic components, and the barotropic streamfunction has to be calculated at each time step and grid point of the model by using a costly successive overrelaxation solver (Andrich et al. 1988). The proposed assimilation method avoids these sensitive points and allows one to obtain a system close to the primitive equations set used in OCMs, but with the added value of being much more simple to be resolved. This technique is original in comparison with those in the past because it assimilates directly the current data instead of the mass fields. The technique is also very useful and efficient in preventing strong drifts during long simulations and shocks associated with sequential assimilation data. Nevertheless some limitations of the approach have to be mentioned.



TABLE 1. Summary of the datasets and analyses used.

Products	Goals	Data → Products
POMME analyses ( $T, S, \mathbf{U}_g$ )	Initialization and boundary conditions	Hydrological surveys: CTD(143), XCTD(13), and XBT(119), for each network
SOPRANE analyses ( $\mathbf{U}_g$ )	Geostrophic currents for the guide	Sea level anomaly. Altimeters: TOPEX/Poseidon, JASON-1, ENVISAT, Geosat, and ERS-1 and -2
Daily SST analyses	To validate the model and compute surface fluxes	NOAA-AVHRR + in situ (thermosalinograph, buoys)
Daily surface fluxes	To force the surface ocean model	Radiative long-wave and short-wave components: Meteosat. Turbulent component: bulk algorithm using the daily SST analyses and the ECMWF atmospheric and precipitation analyses

Geostrophic currents have to be provided with a forecasting/analysis system or climatologies. Consequently, this model is only viable when nested with a geostrophic currents provider. Sampling of in situ data over a domain induces space and time aliasing and nonsynopticity in the analyzed fields that in turn can affect the realism of the simulated structures. Such kind of problem can be removed when primary observations and model data are combined in a series of linked cycles (Robinson et al. 1996). The geostrophic guide is built by linear interpolation between two analyzed geostrophic current fields. When the analyzed fields are distant from each other, the linear interpolation can be a rough hypothesis. When the model is implemented in a region where experimental data are not available, geostrophic currents can be deduced from climatologies, OGCMs, or altimetric dynamic heights. Realism of simulated structures highly depends on the guide realism, which can be very rough, especially in climatologies. When altimetric analyses are available only surface geostrophic currents can be derived. The altimetric signal has to be projected onto climatological vertical modes (EOFs) in order to deduce the vertical geostrophic currents (Gavart et al. 1999). Such currents have a statistical validity but can be distant from the real case considered.

### 3. Model Implementation in POMME area

The treatment of the open lateral and surface boundaries is presented in appendix B.

#### *Analyses and implementation*

The main part of the experiment took place from August 2000 to October 2001, with four oceanographic cruises during which two vessels were used each time (*Atalante* and *d'Entrecasteaux*) to perform hydrological surveys at 50-km resolution, nearly 2 times the internal Rossby radius of deformation, 20 km, deduced from the data used in this experiment.

A large variety of analyses have been produced to document the mass fields and circulation during the POMME experiment, which are summarized in Table 1 and briefly presented herein.

Hydrological surveys were used to produce high-resolution temperature and salinity analyses (hereinaf-

ter called POMME analyses). These data were first interpolated onto 65 vertical levels (of 5-m vertical resolution near the surface, 300 m at depth) and then objectively analyzed onto a 5-km horizontal grid for all vertical levels following the procedure used by Caniaux and Planton (1998) and Dourado and Caniaux (2001). The first guess of the analyses was derived from the temperature and salinity Levitus (1982) climatology. At each grid point, the climatology was corrected using observations that lie within one influence time-space radius around the grid point, following the procedure of De Mey and Ménard (1989). A space correlation radius of 50 km, consistent with the mesoscale structures, and a decay  $e$ -folding time of 10 days were chosen (following a compromise between salinity and temperature data) in order to time center each analysis to each midsurvey date. Analyses were thus produced on 28 September 2000 (POMME0), 13 February 2001 (POMME1), 4 April 2001 (POMME2), and 4 September 2001 (POMME3) corresponding to the middle dates of the four intensive observing periods, respectively. From these analyses, geostrophic currents were computed at each level through the thermal-wind equation by using a level of no motion. The determination of a level of no motion represents a problem; several tests were performed in order to adopt a compromise, including comparisons with acoustic Doppler current profiler (ADCP) data. The results obtained indicate that (i) varying the level of no motion from 800 to 1870 m (the highest point of the topography) affects the maximum currents with an increase with the depth, (ii) a limitation of the minimum level of no motion is to be under the level of direct influence of Mediterranean water features like meddies, and (iii) in comparison with ship ADCP data, the best statistics were obtained with a level of no motion located near 1500 m, which is close to the determination of Stramma (1984) for the region considered in this paper. To use XBT information, salinities were reconstructed from XBT temperatures by using a cubic temperature–salinity ( $T$ – $S$ ) relationship only for North Atlantic Central Waters and under the seasonal thermocline, thus not altering water masses. This relationship (Arhan 1990) was established from the available CTD and applied to the temperature of XBT to reconstruct the salinity.

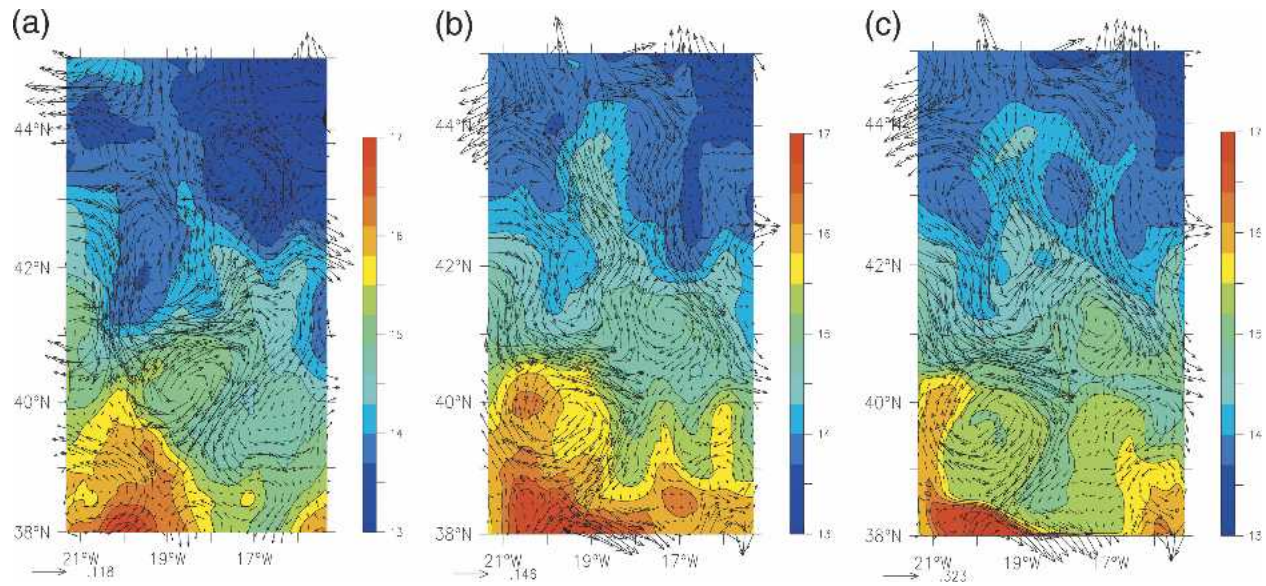


FIG. 4. Analyzed SST ( $^{\circ}\text{C}$ ) and surface geostrophic current ( $\text{m s}^{-1}$ ) at (a) POMME1 and (b) POMME2. (c) Simulated SST ( $^{\circ}\text{C}$ ) and surface current ( $\text{m s}^{-1}$ ) at POMME2 (full physics simulation).

Concurrently, during the year of the experiment, altimeter observations (see Table 1) were assimilated in the QG circulation model SOPRANE (Dombrowsky and DeMey 1992) in order to provide analyses of the streamfunction every week (hereinafter called SOPRANE analyses) over a large domain shown Fig. 1. Given their high frequency of availability, these analyses are not too much affected by nonsynopticity. Gaps between the observed and SOPRANE streamfunctions were objectively analyzed on the SOPRANE grid of 10 vertical levels and 50-km horizontal resolution. The corrected field is then applied to the SOPRANE field. Analyses are centered in a temporal window of 15 days width and the error temporal covariance is Gaussian. The spatial covariance is isotropic with a correlation radius of 50 km. SOPRANE analyses geostrophic currents were derived from the analysis streamfunctions over the simulation domain by finite differencing.

In addition, a large amount of satellite-derived SST was available. These data were corrected, treated, aggregated at the scale of the grid model (5 km), and merged with in situ surface data in order to produce SST objective analyses every 3 days during 1 yr (hereinafter called satellite analyses; see Caniaux et al. 2005).

The POMME, SOPRANE, and satellite SST analyses were produced over grids of high resolutions and at high frequency (see Table 1). In this paper, these products are used for running and validating the model presented in section 2.

This model is implemented in the POMME area extending from 21.33° to 15.33°W and from 38° to 45°N (Fig. 1). The horizontal regular grid spacing is equal to the analysis resolution ( $\Delta x = \Delta y = 5$  km). There are 19

vertical levels covering a total depth of 1000 m with the first at 1 m below the surface and a grid mesh interval ranging from 10 m near the surface and 100 m near the bottom considered as flat.

POMME1 and POMME2 analyses include the most complete hydrological networks among the four intensive observing periods. Moreover, this period of 50 days is probably the best since detrainment of the mixed layer waters occurs effectively over this length. Consequently, it was decided to run the model between POMME1 and POMME2 because this period is important in relation to the project objectives.

#### 4 The “full physics” simulation

##### a. Initialization and ocean forcing

This section is devoted to describing simulation results obtained by activation of all physical processes (“full physics”) into the model. The full physics simulation is initialized with the temperature and salinity analyses produced at POMME1 (13 February 2001) and integrated up to POMME2 (4 April 2001) using daily surface heat fluxes and geostrophic currents linearly interpolated at each time step of the model between two analyses, POMME–SOPRANE and SOPRANE–SOPRANE. The QG system SOPRANE produces the slow manifold of the circulation used as background in our simplified model, which simulates the rapid and small-scale physics (upper active mixed layer, ageostrophic circulations in fronts, and eddies).

At POMME1 (Fig. 4), a surface thermal and circulation front is present around 41°N. This front is associated with two mesoscale eddies. The first is a big cold-

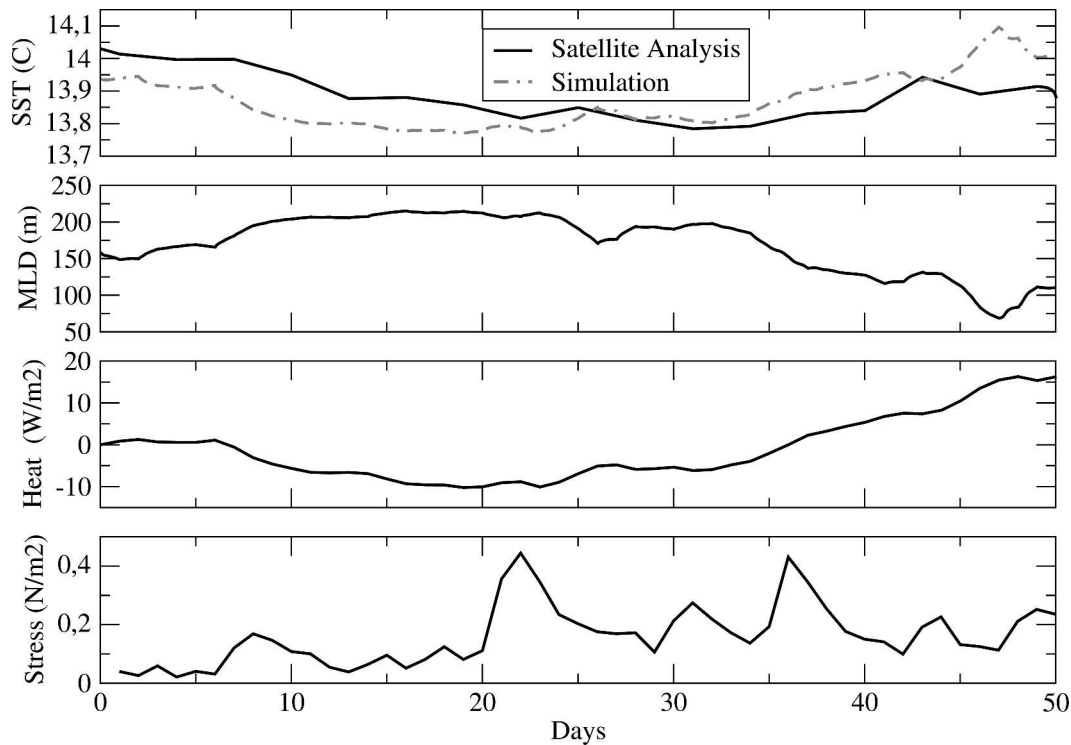


FIG. 5. (top to bottom) Spatial averages of SST, mixed layer depth, net surface heat flux, and surface momentum flux during POMME1–2.

core ( $13^{\circ}\text{C}$ ) cyclonic eddy of 100-km diameter centered at  $42^{\circ}\text{N}$ ,  $20^{\circ}\text{W}$ , and the second is a warm-core ( $15^{\circ}\text{C}$ ) anticyclonic eddy of 60-km diameter centered at  $40^{\circ}\text{N}$ ,  $19^{\circ}\text{W}$ . Current velocities of up to  $0.3\text{ m s}^{-1}$  were found in the front between the two eddy structures. Farther north, a cold-core anticyclonic eddy of 50-km diameter is located at  $43.5^{\circ}\text{N}$ ,  $17.5^{\circ}\text{W}$ . Last, along  $20^{\circ}\text{W}$ , a  $16^{\circ}\text{C}$  water tongue spreads northward in the southwestern part of the domain while in the eastern area lower SSTs ( $14^{\circ}\text{C}$ ) are observed.

#### b. SST and surface currents

The simulated SST obtained at POMME2 (Fig. 4), averaged over the domain, is  $0.2^{\circ}\text{C}$  warmer than the initial field at POMME1 (Fig. 4). SSTs are on the order of  $15^{\circ}\text{C}$  south of  $40^{\circ}\text{N}$ , while a warmer tongue of water ( $16^{\circ}\text{C}$ , 36 psu) in the southwest of the domain ( $20^{\circ}$ – $21^{\circ}\text{W}$ ) extends northward up to  $40^{\circ}\text{N}$ . The SST gradient and associated meandering jet present at POMME1 near  $41^{\circ}\text{N}$  have shifted southwestward at POMME2. North of  $41^{\circ}\text{N}$ , SSTs are lower than  $14^{\circ}\text{C}$  and are minimum in the northeast ( $13^{\circ}\text{C}$ ). A northward warm-water intrusion (not present at POMME1) of  $14^{\circ}\text{C}$  along  $19^{\circ}\text{W}$  appears in the north of the domain. Concurrently, a cold-water descent was observed in the northeastern area, transporting  $13.5^{\circ}\text{C}$  water along  $16.5^{\circ}\text{W}$ .

Simulated surface currents at POMME2 (Fig. 4) highlight significant evolutions of the mesoscale struc-

tures during POMME1–2. The meandering jet has developed a northward branch, which is responsible for the northward warm-water intrusion and a southward branch starting at  $44^{\circ}\text{N}$ , responsible for the cold-water advection. These two branches are connected by a weak eastward current at  $41.5^{\circ}\text{N}$  due to the presence of a small warm-core anticyclonic eddy located at  $41^{\circ}\text{N}$ ,  $17^{\circ}\text{W}$ . Cyclonic and anticyclonic eddies identified at POMME1 in the southwest area (Fig. 4) have moved to the southwest whereas the anticyclonic eddy in the northeast only deformed.

A very intense mesoscale activity was found during POMME1–2 because structures moved and became deformed. Such deformations, induced by geostrophic large-scale forcing and interactions between structures at mesoscale, generate vertical velocities, which are suspected to play a role as important as the surface fluxes in subducting water.

When averaged over the domain, behaviors of the mixed layer depth [MLD, defined as  $\Delta\rho = \rho(z) - \rho(20\text{ m}) = 0.02\text{ kg m}^{-3}$ ; see section 5a] and net surface heat flux have some similarities as shown in Fig. 5. A sharp decrease of the MLD in the second half of the simulation is clearly associated with a significant increase in the net surface heat flux. Positive net surface heat flux in the last-third part of the simulation induces a marked restratification and warming (SST) of the mixed layer. Surface stress displays two strong events at days 22 and



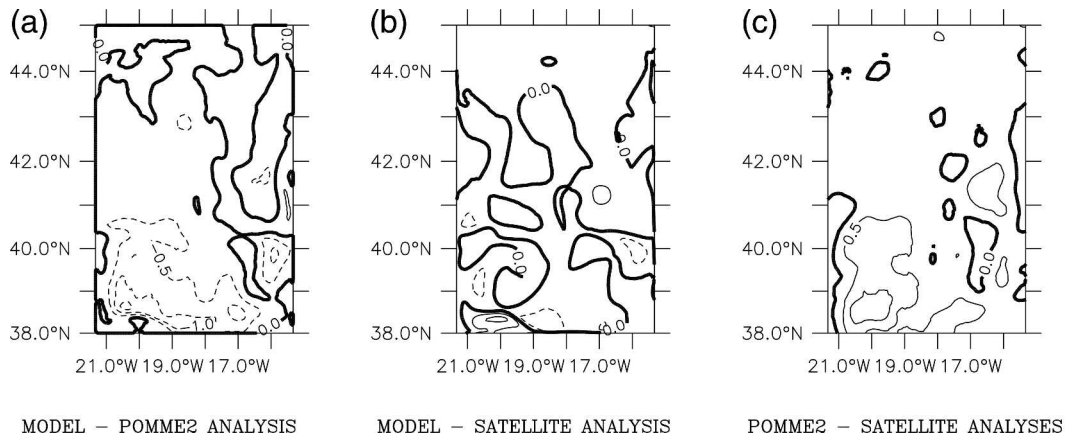


FIG. 6. Errors ( $^{\circ}\text{C}$ ) of the final simulated SST as compared with (a) POMME2 and (b) satellite analysis. (c) SST difference between the POMME2 and satellite analyses.

36, nevertheless these atmospheric events are short-lived and do not affect the mixed layer characteristics significantly because the mixed layer is thick ( $>100$  m) and has thus a great inertia. Therefore at least at synoptic scale, the MLD seems to be driven by the atmospheric heat forcing. This result stresses the need to have accurate surface fluxes mainly in cases of shallow MLDs.

## 5. Validation

### a. Mass fields

The simulated SST and current structures obtained at POMME2 (Fig. 4) are close to those analyzed (Fig. 4). The front at  $41^{\circ}\text{N}$  is well described and the northward/southward branches, which transport warm/cold waters, are also well simulated. The simulated surface currents include all the physical processes and particularly atmospheric surface stress impacts. This is the reason why the simulated currents are stronger than those analyzed which are geostrophic. The water pass connecting these two branches is particularly well represented by the simulation because of a good simulation of the anticyclonic eddy located at  $41^{\circ}\text{N}$ ,  $17^{\circ}\text{W}$ . This performance is noteworthy because scale of these structures is small.

Relative to POMME2 and satellite SST analyses, model errors are negative ( $-1^{\circ}\text{C}$ ) and positive ( $1^{\circ}\text{C}$ ), respectively. Consequently some differences exist between the two SST references (Fig. 6). Negative bias found in the southwest part of the domain is associated with the nonsynopticity of the POMME2 analysis. Indeed, this analysis includes in situ data spread over 20 days and the measurements located in the southwest were collected around 20 April. Consequently, on 4 April, the POMME2 analysis could have overestimated the SST in this region. Relative to the satellite analysis, model errors are often less than  $0.5^{\circ}\text{C}$  over the domain that falls in the range of the analysis and data uncer-

tainties. As compared with the POMME2 analysis, daily SST satellite analysis is not contaminated by nonsynopticity effects and compares quite well to simulation. This result indirectly shows that the assimilated SOPRANE geostrophic currents are not too much contaminated by nonsynopticity effects. Relative to POMME1, the hydrological network POMME2 is much more affected by nonsynopticity effects because its shallowest mixed layer depth gives to surface parameters greater reactivity to atmospheric surface forcings. To some extent of rough initial conditions, the mass field should become realistic because of the geostrophic adjustment process and good atmospheric surface fluxes. The geostrophic guide gives the system a short memory of the previous states.

As a result of the realistic assimilated geostrophic currents, it can be concluded that the final simulation catches the mesoscale structures well. For instance, the thermohaline front in the west and eddy associated with the meridional circulation in the northeastern part of the domain are described with good accuracy (Fig. 4).

When averaged over the domain, the simulated SST is colder than the satellite up to day 25 (Fig. 5) and conversely beyond. Initial SSTs are different because the satellite and POMME1 analyses have not assimilated the same observations; nevertheless, the spatial structures are identical (not shown). At POMME2, the simulated SST is  $0.2^{\circ}\text{C}$  warmer than that from the satellite. This difference is small but probably means that the surface heat budget has a positive bias.

Analyzed and simulated vertical structures of temperature and salinity are shown along the cross section that starts at  $38^{\circ}\text{N}$  and ends at  $45^{\circ}\text{N}$  along  $18^{\circ}\text{W}$  (Fig. 7). The main structures of analyzed temperature and salinity are well described in the simulation, particularly the thermohaline front located at  $42.5^{\circ}\text{N}$ . The mixed layer depth is estimated at 50 m except in the front where it reaches 100 m. Nevertheless, some disparities exist between the analyzed and simulated



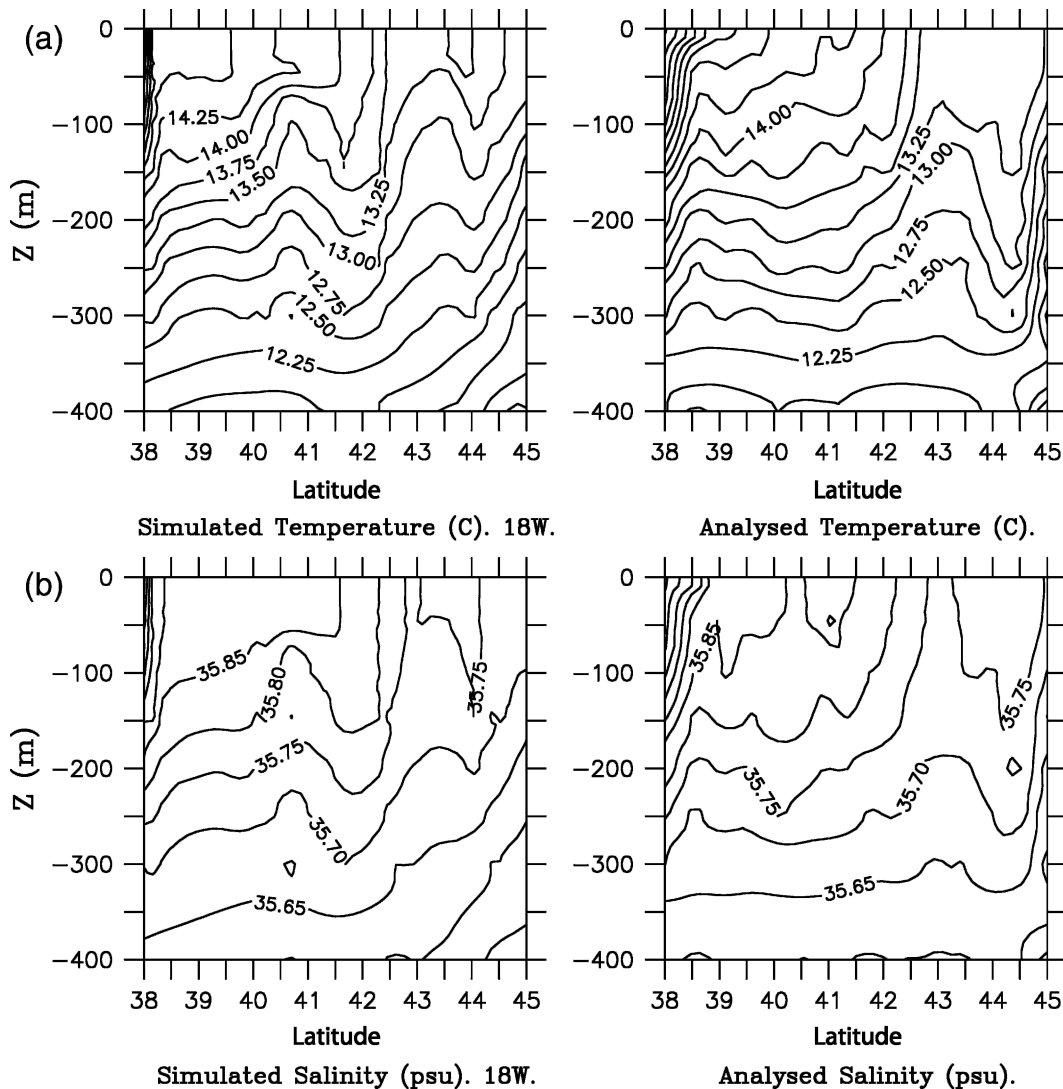


FIG. 7. (a) Vertical cross section of (left) simulated and (right) analyzed temperature ( $^{\circ}\text{C}$ ); (b) same as (a) but for (left) simulated and (right) analyzed salinity (psu) at  $18^{\circ}\text{W}$ .

fields, as for instance in the temperature pattern around  $40.5^{\circ}\text{N}$  where the model simulates an ascent of cold water, which does not appear in the POMME2 analysis.

An MLD reference was visually estimated from each observed density sounding used to perform the POMME2 analysis (Fig. 8). This method is thus independent from any subjective numerical criterion, which is a real advantage. Nevertheless, as the analyses fields, the MLD reference is also affected by the nonsynoptic of the measurements and some structures are certainly not time coherent. Consequently, derived observed fields have to be considered as composite pictures. Simulated MLDs were deduced through a density criterion, which is defined by a density gap between the current level and the level  $z = 20$  m equal to  $0.02 \text{ kg m}^{-3}$  according to the numerous tests performed

by the POMME community (Paci et al. 2005; Levy et al. 2005). A linear interpolation between levels is used to estimate the exact depth at which the difference criterion is reached. Level  $z = 20$  m was chosen to avoid a large part of the skin effects (Price et al. 1986). The MLD based on a density difference criterion was preferentially chosen because it is more stable than the MLD based on a gradient criterion (Brainerd and Gregg 1995). The spatiotemporal stability was reached reasonably with the density gap mentioned above. MLD structures are thus very difficult to estimate because this derived field is highly sensitive to the criteria used, and consequently, many differences between the simulated and observed fields can rise. Despite these difficulties, maxima in the northwestern corner, relative maxima in the west and southwest, and relative minima

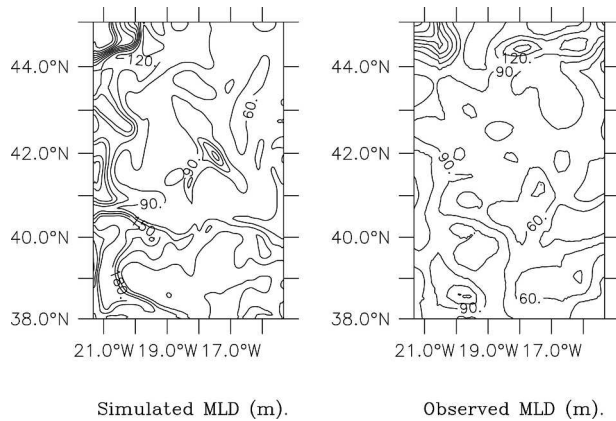


FIG. 8. (left) Simulated and (right) observed mixed layer depths at POMME2.

located in the southeast of the domain are captured by the simulation.

### b. Dynamic fields

The simulated circulation was validated with the surface drifting buoy trajectories captured in the domain during POMME1–2. These trajectories were superimposed onto the simulated dynamic height (DH) and are shown Fig. 9. These days correspond approximately to the central time of the trajectories, and the DH fields were computed with respect to level 1000 m. On 10 March, the anticyclonic eddy in the north, the front, and the recirculation branch around the anticyclonic eddy in the south of the domain are found in phase in the simulation and in the buoy trajectories. On 30 March,

the deformation field—prescribed by the geostrophic forcing—induced a north–south stretch in the DH field in comparison with 10 March, shown well by the buoy trajectory at 42°N. Such frontogenesis zones have to be realistic because their role in the detrainment/entrainment water process induced by vertical velocity could be important (Hiroyuki and Yasuda 2004). Last, on 20 March, trajectories in the eastern part of the domain are not so close to the altimeter topography, suggesting a possible action of the wind and/or the inertial currents on the drifting buoys. In conclusion, the model catches the fine dynamical structures described by the buoy trajectories quite well.

## 6. Sensitivity to the processes activated

As mentioned previously, the model has a very interesting modularity in research mode. This modularity is now illustrated by the simulated SST and surface current fields obtained at POMME2, each one deduced from the previous by adding one new physical process. Four sensitivity tests are presented in this section and are defined and summarized in Table 2 and presented in Figs. 10 and 4.

When the vertical diffusion is the only process activated (DIF), the mixed layer evolves only under the surface heat and momentum forcings. In such conditions, structures of the final simulated SST field are close to the initial analyzed SST field because the atmospheric forcing affects the mixed layer uniformly over the domain during POMME1–2 and induces weak deformations. In this case, the surface Ekman current, induced by the surface momentum forcing, does not act on the prognostic variables of the model, but is taken into account in the vertical diffusion. This pattern

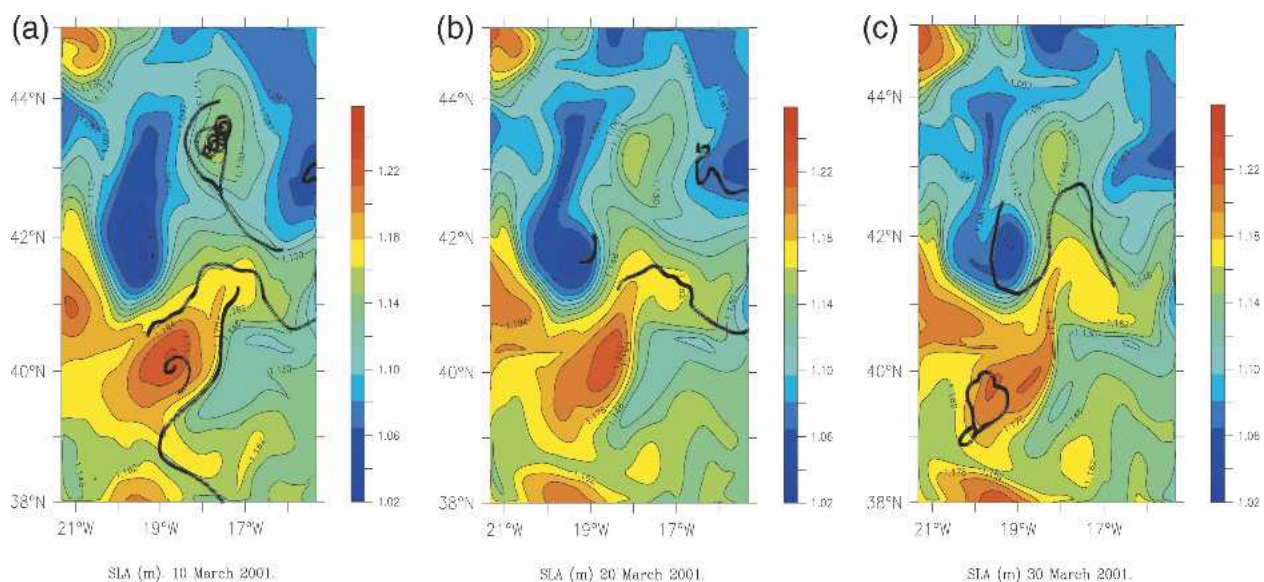


FIG. 9. Simulated dynamic height (m) and buoy trajectories on (a) 10, (b) 20, and (c) 30 Mar.

TABLE 2. Definition of the sensitivity tests. Horizontal and vertical currents mentioned in the column “processes activated” correspond to the activation of momentum and thermodynamic advections.

Acronyms	Processes activated
DIF	Diffusion
DIF-EK	Diffusion + Ekman current
DIF-EK-GEO	Diffusion + Ekman + geostrophic currents
FULL-PHYSIC	Diffusion + Ekman + geostrophic currents + vertical velocity

shows that the surface wind was southwesterly at POMME2. When both the vertical diffusion and advection by the Ekman current are activated simultaneously (DIF-EK), vertical processes become coupled to the each other and the SST structures are much more coherent than in DIF. In this case, the Ekman current feedbacks on itself and produces SST and surface current patterns very different than in DIF, so that it is no longer possible to identify the wind effect on the surface current. Consequently, experiments DIF and DIF-EK allow the quantification of impacts of the Ekman current on the SST field but also the retroaction loop on itself. This feedback is strong and also has consequences on the vertical diffusion since it induces turbulent kinetic energy by vertical shear. When the geostrophic current is added to the processes activated in experiment DIF-EK, SST and current structures simulated at POMME2 (DIF-EK-GEO) become drastically different because the geostrophic forcing is a strong dynamical component in this region. Main SST and current structures are still close to those analyzed as shown

Fig. 4. Note that the simulated surface current is different in intensity and structure in comparison with the geostrophic current because of the horizontal ageostrophic processes. The stronger simulated current intensities ( $0.3 \text{ m s}^{-1}$  in the front) relative to the geostrophic current is more realistic in comparison with surface drifting buoys. The Ekman current is still different from that in DIF-EK (not shown), and it may be possible to know the nonlinear action of the geostrophic forcing on the Ekman/ageostrophic current. When the vertical advections are added to the processes activated in the experiment DIF-EK-GEO, the model runs with its full physics. Simulated SST and current are slightly modulated in comparison with those in DIF-EK-GEO (Figs. 10 and 4). The vertical advections tend to cool the mixed layer temperature and allow the best SST score to be reached in comparison with the satellite analysis.

## 7. Summary and conclusions

This paper presents an original simplified three-dimensional model obtained by the assimilation of analysis-derived geostrophic currents into the momentum equation by substitution of the horizontal pressure gradient. In this system, simplification is provided by the temporal sequence of  $\mathbf{U}_g$  called guide, which is used as a low-resolution and low-frequency interpolator. This guide represents the slow manifold of the dynamics. This model is thus necessarily coupled to systems providing geostrophic currents—that is, OCMs, analyzed/reanalyzed fields, or climatologies. This model is thus an alternative approach of regional forecasting

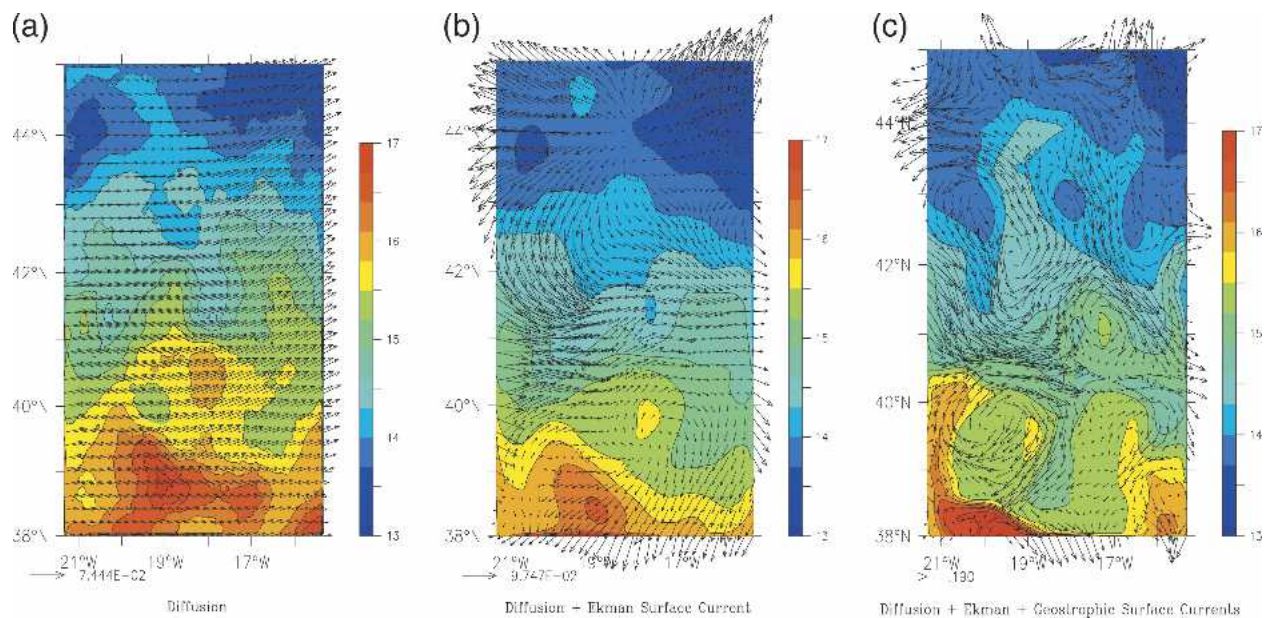


FIG. 10. Simulated SST ( $^{\circ}\text{C}$ ) and surface current ( $\text{m s}^{-1}$ ) at POMME2: (a) the vertical diffusion activated, (b) vertical diffusion and Ekman advections activated, and (c) vertical diffusion and Ekman-geostrophic advections activated.



that benefits from outputs of advanced forecasting/assimilating systems. The temporal sequence of analyzed geostrophic currents was assimilated at each model time step, thus continuously, by using a direct insertion technique. This assimilation technique gives the possibility to study the development of simulated structures as a function of the mesoscale environment, in particular the scales smaller than the Rossby radius. By not computing the pressure, this model is thus a degenerate PE system that does not generate gravity waves and in which geostrophic structures have an effect on ageostrophic structures but not vice versa. Under these conditions, the mass field adjusts to the prescribed geostrophic field through the thermodynamic equations. The gradual assimilation of geostrophic currents into the model allows it to (i) avoid shocks and spin up following sequential assimilation data, (ii) avoid a strong drift of the model during long-term simulations, (iii) perform time-integrated physical diagnoses, and (iv) independently activate vertical diffusion, and horizontal and vertical advections.

Simulations of 50 days between POMME1 and POMME2 of the POMME experiment have shown that the model is very realistic in terms of representing thermodynamic and circulation structures at the mesoscale when verifying against analyses and observations. The geostrophic guide impedes the model drift and could allow very long simulations to be performed with hope of realistic predictions when using suitable surface heat and momentum forcing.

Sensitivity tests allowing the study of structure development under a given mesoscale context can probably be better investigated in the proposed model than in PE systems. For illustration, some retroaction loops have been identified by performing a series of sensitivity tests corresponding to a sequential activation of the processes that three-dimensionalize the model step by step. This model allows for the quantification of the nonlinear impact of one process on others, and ultimately understanding of how the processes set up and interact between themselves when activated online. Simulated mesoscale structures become realistic when geostrophic forcing is activated. Therefore, geostrophic forcing also induces realistic geostrophic adjustment. Activation of the vertical velocity improves the final solution that proves the realistic evolution of the structures during the simulation. The  $w$  impact does not appear to be significant but could be more important for longer simulations.

No statistical uncertainties were used in the assimilation method, but this guided system could be softened by blending the forecast and the analyzed geostrophic currents in connection with their uncertainties. In this case, the ageostrophic structures could have a retroaction on the geostrophic ones that corresponds to activating an additional degree of freedom of the system. This model has to be considered a complementary numerical tool when compared with OCMs, and also as a

benchmark to test ideas about assimilation in a simplified framework. Nested onto an operational OCM equipped with a data assimilation system, this model could be used to perform computationally cheap real-time forecasts with higher resolutions in regional domains (downscaling) for operations, research, and management purposes.

One of the main goals of the POMME experiment is to evaluate mode water production and circulation in the northeast Atlantic. Such objectives require realistic 1-yr 3D simulations. This model is a specially adapted numerical tool that reaches this objective. Consequently, heat and mass budgets and processes driving subduction–obduction at the mesoscale and submesoscale during POMME will be investigated with this model and presented in a forthcoming paper.

*Acknowledgments.* The authors acknowledge the SHOM/CMO for giving its authorization to use and publish the QG model results from SOPRANE system in a scientific framework. The analysis simulations have been done by S. Giraud from CLS under contract (01.87.009.00.470.29.25) with SHOM/CMO.

We are most grateful to Youcef Amar for his valuable technical assistance and to Robin Clark for his help in revising this manuscript. We are grateful to the scientific staff M. Bianchi, G. Reverdin, and L. Mémerly for their managing of the POMME experiment.

We thank Pierre Lermusiaux and the anonymous reviewer for their comments that helped to significantly clarify and improve this paper.

This work was supported by the French programs PATOM and PROOF (CNRS/INSU).

## APPENDIX A

### Numerical Resolution of the Degenerate PE System

The model's system of equations in Eq. (8) is finite differenced on a horizontal and vertical staggered grid. The trends of the prognostic variables  $U_h$ ,  $T$ ,  $S$  and  $e_T$  are computed using the Euler forward time scheme. The vertical momentum, temperature, salinity and turbulent kinetic energy diffusion including the surface forcing in the prognostic equations are considered implicitly (i.e., at the next time step,  $t + \Delta t$ , where  $\Delta t$  is the model time step) when the other terms are considered explicitly (i.e., at the current time  $t$ ). The Coriolis force is split into implicit and explicit parts in order to simulate a realistic inertial mode. Horizontal and vertical advections of the prognostic variables are finite differenced using an upstream scheme (Lapudis and Pinder 1982) and the forcing terms of  $e_T$  in Eq. (2) are finite differenced using a centered scheme, except the vertical transport. These choices ensure a good stability and consistence of the numerical scheme. In these conditions, the prognostic equations of the system of Eq. (8) are written as an implicit linear system  $\mathbf{A}\mathbf{X}^{t+\Delta t} = \mathbf{Y}^t$ , where  $\mathbf{A}$  is a tridiagonal matrix,  $\mathbf{X} = (U_h, T, S, e_T)$  is the



state vector, and  $\mathbf{Y}$  is the explicit second member. Last,  $\mathbf{X}^{t+\Delta t}$  is computed by inversion of matrix  $\mathbf{A}$  (for more details, see Gaspar et al. 1990).

The vertical velocity is diagnosed from the vorticity equation where the advection of vorticity and the baroclinic terms are finite differenced using an upstream scheme and the tilting and stress terms are finite differenced using a centered scheme. The local trend of vorticity is computed with a backward time scheme. The vertical velocity is computed at each level of the vertical grid by integration of Eq. (6) [fourth equation from top of Eq. (8)] from the bottom ( $w = 0$ ) up to the surface.

## APPENDIX B

### Boundary Conditions

#### a. Open lateral boundaries

One of the main difficulties in modeling a limited area of the ocean is the treatment of open lateral boundaries. One of the most pragmatic numerical methods consists of modifying the prognostic equations in a zone close to the boundary. As in Caniaux and Planton (1998), a Newtonian relaxation can be applied to the prognostic variables  $X$  in a zone near the boundary toward a large-scale field  $\tilde{X}(i)$  with a damping coefficient  $\alpha(i)$  both varying with distance  $i$  from the lateral boundary. Following Leslie et al. (1981), if  $X_p$  is the prognostic part of the model, the final solution  $X_f$  is found using the following relation:

$$X_f = [1 - \alpha(i)]X_p + \alpha(i)\tilde{X}(i),$$

$$\text{where } 0 \leq \alpha(i) \leq 1 \quad \text{for } 1 \leq i \leq N_{\text{relax}},$$

where  $N_{\text{relax}}$  is the number of relaxed rows. Numerous tests were performed to define the subdomain of relaxation minimizing the intensity and propagation of spurious numerical gravity waves in the simulation domain. These tests lead to choose  $N_{\text{relax}} = 1$  and  $\alpha(1) = 1$ . Thus no Newtonian relaxation was performed and only boundary values were held equal to the large scale field  $\tilde{X}(i)$ . Consequently, the large-scale information prescribed on the boundaries propagates inside the domain through the advections. The specified values  $\tilde{X}(i)$  on the boundaries of the simulation domain may be held constant in time or may be allowed to evolve. In the reported experiment a tendency has been added to each  $\tilde{X}(i)$  because of significant evolution of the temperature and salinity during POMME1–2. However, because of the lack of large-scale information during the simulation, these tendencies were obtained by linear interpolation between the initial and final analyses POMME1 and POMME2, respectively.

#### b. Surface atmospheric forcing

Different datasets were used for surface net heat fluxes (see Table 1). Hourly surface irradiances (solar

and downward longwave radiation fluxes) were derived from the geostationary Meteosat satellite dataset collected at the Center de Météorologie Spatiale (Météo-France, Lannion) following the method developed by Brisson et al. (1994). Radiation fluxes available at 4 km of resolution were aggregated on the model grid space.

Daily sea surface temperature (SST) analyses were computed on the grid model by assimilation of advanced very-high resolution radiometer (AVHRR) data available at 2 km of resolution. Upward longwave radiation fluxes were computed from the analyzed SSTs.

Atmospheric parameters of the European Centre for Medium-Range Weather Forecasts (ECMWF) analyses available every 6 h were interpolated onto the model grid and combined with analyzed satellite SSTs to compute the heat and momentum surface turbulent fluxes. These fluxes were obtained with the use of a specific state-of-art bulk algorithm developed with the turbulence data collected during the experiment (Caniaux et al. 2005).

Time series of turbulent heat and momentum forcings display strong intermittencies, which are associated with the passage of atmospheric depressions over the domain. Because of the high resolution of the SST and atmospheric analyses, mesoscale structures of the turbulent surface fluxes were restored (see Caniaux et al. 2005).

The surface is forced with these daily estimates of penetrative solar radiation, radiative cooling, evaporation minus precipitation, sensible heat flux, and wind stress.

## REFERENCES

- Andrich, P., P. Delecluse, C. Levy, and G. Madec, 1988: A multitasked general circulation model of the ocean. *Science and Engineering on Cray Supercomputer: Proc. of the Fourth Int. Symp.*, Minneapolis, MN, Cray Research, Inc., 407–428.
- Arhan, M., 1990: The North Atlantic Current and Subarctic Intermediate Water. *J. Mar. Res.*, **48**, 109–144.
- Blanke, B., and P. Delecluse, 1993: Variability of the tropical Atlantic Ocean simulated by a general circulation model with two different mixed-layer physics. *J. Phys. Oceanogr.*, **23**, 1363–1388.
- Bougeault, P., and P. Lacarrère, 1989: Parameterization of orography-induced turbulence in a meso-beta scale model. *Mon. Wea. Rev.*, **117**, 1872–1890.
- , and R. Sadourny, 2001: *Dynamique de l'atmosphère et de l'océan*. Edition de l'Ecole Polytechnique, Département de Mécanique, 235 pp.
- Brainerd, K. E., and M. C. Gregg, 1995: Surface mixed and mixing layer depths. *Deep-Sea Res.*, **9**, 1521–1543.
- Brisson, A., P. Leborgne, A. Marsouin, and T. Moreau, 1994: Surface irradiances calculated from Meteosat sensor data during SOFIA-ASTEX. *Int. J. Remote Sens.*, **15**, 197–203.
- Caniaux, G., and S. Planton, 1998: 3D ocean mesoscale simulation using data from the SEMAPHORE experiment: Mixed layer heat budget. *J. Geophys. Res.*, **103**, 2581–2599.
- , A. Brut, D. Bourras, H. Giordani, A. Paci, L. Prieur, and G. Reverdin, 2005: A one-year sea surface heat, freshwater, and momentum budget in the northeastern Atlantic Basin during the Pomme Experiment: Part I: Flux estimates. *J. Geophys. Res.*, in press.

- Daley, R., 1981: Normal mode initialisation. *Rev. Geophys. Space Phys.*, **19**, 450–468.
- De Mey, P., and Y. Ménard, 1989: Synoptic analysis and dynamics adjustment of GEOS-3 and *Seasat* altimeter eddy fields in the northwest Atlantic. *J. Geophys. Res.*, **94**, 6221–6230.
- Dombrowsky, E., and P. De Mey, 1992: Continuous assimilation in an open domain of the northeast Atlantic. I: Methodology and application to Athena-88. *J. Geophys. Res.*, **97**, 9719–9731.
- Dourado, M. S., and G. Caniaux, 2001: Surface heat budget in an oceanic simulation using data from TOGA COARE. *J. Geophys. Res.*, **106**, 16 623–16 640.
- Gaspar, P., Y. Grégoris, and J. M. Lefevre, 1990: A simple eddy kinetic energy model for simulations of the oceanic vertical mixing: Tests at Station Papa and long-term upper ocean study site. *J. Geophys. Res.*, **95**, 16 179–16 193.
- Gavart, M., 1996: Modélisation et assimilation de données dans un modèle de circulation océanique à méso-échelle: Application à la campagne SEMAPHORE. Ph.D. thesis, Université Paul Sabatier.
- , and P. De Mey, 1997: Isopycnal EOFs in the Azores current region: A statistical tool for dynamical analysis and assimilation. *J. Phys. Oceanogr.*, **27**, 2146–2157.
- , —, and G. Caniaux, 1999: Assimilation of satellite altimeter data in a primitive-equation model of the Azores–Madeira region. *Dyn. Atmos. Oceans*, **29**, 217–254.
- Giordani, H., and S. Planton, 2000: Modeling and analysis of ageostrophic circulation over the Azores oceanic front during the SEMAPHORE experiment. *Mon. Wea. Rev.*, **128**, 2270–2287.
- Hamming, R. W., 1989: *Digital Filters*. Prentice Hall, 284 pp.
- Hiroyuki, T., and T. Yasuda, 2004: Formation and circulation of mode waters of the North Pacific in a high-resolution GCM. *J. Phys. Oceanogr.*, **34**, 399–415.
- Holton, J. R., 1979: *An Introduction to Dynamic Meteorology*. International Geophysics Series, Academic Press, 392 pp.
- Josse, P., 1999: Modélisation couplée Océan-Atmosphère à méso-échelle: Application à la campagne SEMAPHORE. Ph.D. thesis, Université Paul Sabatier, 226 pp.
- Kantha, L. H., and C. A. Clayson, 1994: An improved mixed layer model for geophysical applications. *J. Geophys. Res.*, **25**, 235–266.
- Lapidus, L., and G. F. Pinder, 1982: *Numerical Solution of Partial Differential Equations in Science and Engineering*. Wiley-Interscience and John Wiley and Sons, 452 pp.
- Large, W. G., J. C. McWilliams, and S. Doney, 1994: Ocean vertical mixing: A review and a model with nonlocal boundary layer parameterization. *Rev. Geophys.*, **32**, 363–403.
- Lermusiaux, P. F. J., 1999: Data assimilation via error subspace statistical estimation. Part II: Middle Atlantic Bight Shelf-break Front simulation and ESSE validation. *Mon. Wea. Rev.*, **127**, 1408–1432.
- , and A. R. Robinson, 1999: Data assimilation via error subspace statistical estimation. Part I: Theory and schemes. *Mon. Wea. Rev.*, **127**, 1385–1407.
- Leslie, L. M., G. A. Miles, and D. J. Gauntlett, 1981: The impact of FGGE data coverage and improved numerical techniques in numerical weather prediction in the Australian region. *Quart. J. Roy. Meteor. Soc.*, **107**, 627–642.
- Levitus, S., 1982: *Climatological Atlas of the World Ocean*. NOAA Prof. Paper 13, 173 pp. and 17 microfiche.
- Lévy, M., M. Gavart, L. Mémerly, G. Caniaux, and A. Paci, 2005: A 4D-mesoscale map of the spring bloom in the northeast Atlantic (POMME experiment): Results of a prognostic model. *J. Geophys. Res.*, in press.
- Lozano, C. J., A. R. Robinson, H. G. Arango, A. Gangopadhyay, N. Q. Sloan, P. J. Haley, and W. G. Leslie, 1996: An interdisciplinary ocean prediction system: Assimilation in strategies and structured data models. *Modern Approaches to Data Assimilation in Ocean Modelling*, Elsevier Oceanography Series, P. Malanotte-Rizzoli, Ed., Elsevier Science, 413–452.
- Lynch, P., 1985a: Initialization of a barotropic limited-area model using Laplace transform technique. *Mon. Wea. Rev.*, **113**, 1338–1344.
- , 1985b: Initialization using Laplace transforms. *Quart. J. Roy. Meteor. Soc.*, **111**, 243–258.
- , 1997: The Dolph–Chebyshev window: A simple optimal filter. *Mon. Wea. Rev.*, **125**, 655–660.
- Machenhauer, B., 1977: On the dynamics of gravity oscillations in a shallow water model, with application to normal mode initialisation. *Beitr. Phys. Atmos.*, **50**, 253–271.
- Paci, A., G. Caniaux, M. Gavart, H. Giordani, M. Lévy, L. Prieur, and R. Reverdin, 2005: A high resolution simulation of the ocean during (POMME experiment). Part I: Simulation results and comparison with observations. *J. Geophys. Res.*, in press.
- Paillet, J., and M. Arhan, 1996: Shallow pycnoclines and mode water subduction in the eastern North Atlantic. *J. Phys. Oceanogr.*, **26**, 96–114.
- Pedlosky, J., 1987: *Geophysical Fluid Dynamics*. Springer-Verlag, 710 pp.
- Price, J. F., R. A. Weller, and R. Pinkel, 1986: Diurnal cycling: Observation and models of the upper ocean response to diurnal heating, cooling and wind mixing. *J. Geophys. Res.*, **91**, 8411–8427.
- Qiu, B., and K. A. Kelly, 1993: Upper-ocean heat balance in the Kuroshio Extension region. *J. Phys. Oceanogr.*, **23**, 2027–2041.
- , —, and T. M. Joyce, 1991: Mean flow and variability in the Kuroshio Extension from *Geosat* altimetry data. *J. Geophys. Res.*, **96**, 18 491–18 507.
- Robinson, A. R., 1996: Physical processes, field estimation and an approach to interdisciplinary ocean modeling. *Earth Sci. Rev.*, **40**, 3–54.
- , H. G. Arango, A. Warn-Varnas, W. G. Leslie, A. J. Miller, P. J. Haley, and C. J. Lozano, 1996: Real-time regional forecasting. *Modern Approaches to Data Assimilation in Ocean Modelling*, Elsevier Oceanography Series, P. Malanotte-Rizzoli, Ed., Elsevier Science, 377–412.
- , P. F. J. Lermusiaux, and N. Quincy Sloan, 1998: Data assimilation. *The Sea, The Global Coastal Ocean*, A. R. Robinson and K. H. Brink, Eds., Vol. 11, John Wiley and Sons, 541–594.
- Rosati, A., and K. Miyakoda, 1988: A general circulation model for upper ocean simulation. *J. Phys. Oceanogr.*, **18**, 1601–1626.
- Stramma, L., 1984: Geostrophic transport in the warm water sphere of the eastern subtropical North Atlantic. *J. Mar. Res.*, **42**, 537–558.
- Viúdez, A., J. Tintoré, and R. L. Haney, 1996: About the nature of the generalized omega equation. *J. Atmos. Sci.*, **53**, 787–795.